Med Biol Eng Comput (2014) 52:827–839
DOI 10.1007/s11517-014-1189-z

ORIGINAL ARTICLE

Unsteady wall shear stress analysis from image-based computational fluid dynamic aneurysm models under Newtonian and Casson rheological models

Marcelo A. Castro · María C. Ahumada Olivares · Christopher M. Putman · Juan R. Cebral

Received: 23 April 2014 / Accepted: 14 August 2014 / Published online: 26 August 2014

Abstract The aim of this work was to determine whether or not Newtonian rheology assumption in image-based patient-specific computational fluid dynamics (CFD) cerebrovascular models harboring cerebral aneurysms may affect the hemodynamics characteristics, which have been previously associated with aneurysm progression and rupture. Ten patients with cerebral aneurysms with lobulations were considered. CFD models were reconstructed from 3DRA and 4DCTA images by means of region growing, deformable models, and an advancing front technique. Patient-specific FEM blood flow simulations were performed under Newtonian and Casson rheological models. Wall shear stress (WSS) maps were created and distributions were compared at the end diastole. Regions of lower WSS (lobulation) and higher WSS (neck) were identified. WSS changes in time were analyzed. Maximum, minimum and time-averaged values were calculated and statistically compared. WSS characterization remained unchanged. At high WSS regions, Casson rheology systematically produced higher WSS minimum, maximum and time-averaged values. However, those differences were not statistically significant. At low WSS regions, when averaging over all cases, the Casson model produced higher stresses, although in some cases the Newtonian model did. However, those differences were not significant either. There is no evidence that Newtonian model overestimates WSS. Differences are not statistically significant.

Keywords Cerebral aneurysms · Angiography · Computational fluid dynamics · Wall shear stress · Casson flow

M. A. Castro (✉)
Grupo de Investigación y Desarrollo en Bioingeniería, Universidad Tecnológica Nacional, Facultad Regional Buenos Aires, CONICET, Medrano 951, CP 1179, Buenos Aires, Argentina
e-mail: marcelo.a.castro@gmail.com

M. C. A. Olivares
Facultad de Ingeniería, Ciencias Exactas y Naturales, Universidad Favaloro, Solís 453, CP 1078, Buenos Aires, Argentina

C. M. Putman
Interventional Neuroradiology, Texas Neurointerventional Surgery Associates, 8210 Walnut Hill, Dallas, TX 75231, USA

J. R. Cebral
Center for Computational Fluid Dynamics, George Mason University, 4400 University Dr., Fairfax, VA 22030, USA

1 Introduction

Since introduced by Taylor et al. [38] and Steinman et al. [36] in 1998, image-based patient-specific computational fluid dynamics (CFD) simulations have been designed and utilized in complex vascular systems to investigate the role of hemodynamics in the development of cerebrovascular pathologies [3, 4, 8, 9, 37]. Different strategies were presented to analyze large data sets [1, 2]. In order to achieve realistic numerical simulations, the vascular geometry must mimic the actual vasculature in the angiography images. A large number of unsupervised or minimally supervised algorithms have been proposed in the past, many of which are based on deformable models, which use image information to recover the shape of the vascular structure [16, 21].

Cerebral aneurysms are abnormal dilatations of the arterial wall whose rupture is associated with high mortality and morbidity rates. The optimal management of unruptured aneurysms is controversial and current decision-making is mainly based on aneurysm size and location.

Current guidelines suggest that large aneurysms and symptomatic unruptured aneurysms should be treated. Incidentally detected aneurysms less than 5 mm in diameter should be managed conservatively, however, small asymptomatic aneurysms also bleed. Therefore, risk indices based on hemodynamic characteristics have been investigated during the last years [3].

There is agreement about the role of wall shear stress (WSS) in the formation, growth and ultimately rupture of cerebral aneurysms [18, 31]. However, controversy still exists about the hemodynamic characteristics that trigger such biomechanical processes. A possible association between high maximum WSS at the systolic peak and rupture in a cohort of 26 anterior communicating artery (AComA) aneurysms has been reported from a patient-specific CFD study [6]. A larger study that included 210 cerebral aneurysms at different locations revealed statistically significant associations between rupture and larger WSS values and concentrations [14]. A connection between the location of aneurysm blebs and the regions of high WSS [13], and high spatial WSS gradient [25] has been also reported. Other investigators reported possible associations between low WSS and either rupture [17, 23, 34] or blister formation [35]. Twenty vascular models harboring aneurysms in the middle cerebral artery were reconstructed and WSS was found to be lower in ruptured aneurysm domes [34]. However, in that study, a limited portion of the parent artery was considered, neglecting important features of the vascular geometry that resulted in a simplified simulated blood flow. Later, it was demonstrated that such simplifications alter intra-aneurysmal flow patterns and increase WSS at the aneurysm domes [4].

Although most previous computational hemodynamics studies assumed a Newtonian viscosity, some have investigated the impact of rheology. A sensitivity study performed over a set of patient-specific image-based CFD models showed that blood rheology does not affect the flow characterization whose association with rupture is investigated [9]. WSS in models of saccular aneurysms was studied using Casson rheology under different flow conditions [20, 24, 29, 32]. Khanafer et al. [24] showed that non-Newtonian WSS is greater during the peak systole in aortic aneurysm models. Rayz et al. [32] found no significant differences between low WSS regions that may be associated with risk of thrombus formation using Newtonian and non-Newtonian CFD simulations in three patient models. However, accounting for non-Newtonian behavior improved the agreement with observations using longitudinal MRI studies. Xiang et al. [41] showed that Newtonian viscosity could overestimate normalized WSS and consequently underestimate the risk of rupture of intracranial aneurysm in three internal carotid artery (ICA) models. In that work, the analysis was performed using a WSS distribution derived from a time-averaged velocity field, which was normalized with respect to a reference value in the parent artery. In a recent work where three WSS metrics were investigated similar normalization and spatially averaging over the aneurysm sac were considered [19].

The aim of this work is to investigate WSS spatial and temporal differences when Newtonian and Casson viscosity models are considered, by means of unsteady finite element blood flow simulations under personalized flow conditions based on flow rate normalization according to the principle of minimum biological work [11] with special interest in the blebs, and distributions at the end diastole, where extremely low WSS is expected. A preliminary work showed in a reduced number of cases that Newtonian WSS estimation was not systematically higher in regions of extremely low WSS at the systolic peak [7]. This work intends to extend that analysis to the end diastole, and regions of low WSS along the cardiac cycle, providing a statistical analysis over a larger number of cases reconstructed from different image modalities. The accuracy of the methodology used in this paper, including image segmentation and blood flow simulations, along with validation and in vivo evaluation studies between CFD and medical image modalities such as four-dimensional phase-contrast magnetic resonance (4D PC-MR) and three-dimensional rotational angiography (3DRA), has been demonstrated in the past [3, 10, 12].

2 Methods

2.1 Vascular imaging and modeling

Ten angiographic images from patients with cerebral aneurysms containing blebs, all in the anterior circulation, were randomly selected from our data base. Aneurysms were located at the bifurcation of the ICA and the posterior communicating artery (PComA), the ICA siphon, the bifurcation of the ICA and the ophthalmic artery, and the anterior communicating artery (AComA) (see Table 1).

Three-dimensional rotational angiography images had been acquired in eight patients with aneurysms in the ICA (cases #1–4, and #6–9) using a Philips Integris System. The others, with aneurysms at the AComA (cases #5) and the ICA Siphon (case #10), had been imaged using four-dimensional computerized tomographic angiography (4DCTA) at 19 time points along the cardiac cycle (Philips Medical Systems, Best, The Netherlands). Each 3DRA 8-s acquisition consisted in 120 projections obtained during a 180° rotation, reconstructed into a 3D dataset of 128^3 voxels covering a field of view of 54.02 mm on a dedicated workstation, while 4DCTA volumes consisted of $512 \times 512 \times 205$ pixels with a spatial resolution of $0.3125 \times 0.3125 \times 0.6125$ mm covering a field of view of $16.0 \times 16.0 \times 12.81$ cm. Images were averaged and masks

Table 1 Location of cerebral aneurysm, aneurysm size, and cross-sectional area of the internal carotid arteries

Case #	Location	Aneurysm size (cm)	ICA cross-sectional area (cm^2)
1	ICA Ophth	0.50	0.150
2	ICA Ophth	0.63	0.138
3	ICA Siph	1.45	0.119
4	ICA Siph	1.30	0.160
5	AComA	0.87	0.170 (right)/0.198 (left)
6	ICA PCom	0.55	0.127
7	ICA PCom	0.85	0.192
8	ICA PCom	0.81	0.147
9	ICA PCom	0.77	0.155
10	ICA Siph	0.85	0.145 (right)/0.144 (left)

ICA Ophth junction of the internal carotid and ophthalmic arteries, *ICA Siph* internal carotid artery siphon, *AComA* anterior communicating artery, *ICA PCom* junction of the internal carotid and posterior communicating arteries

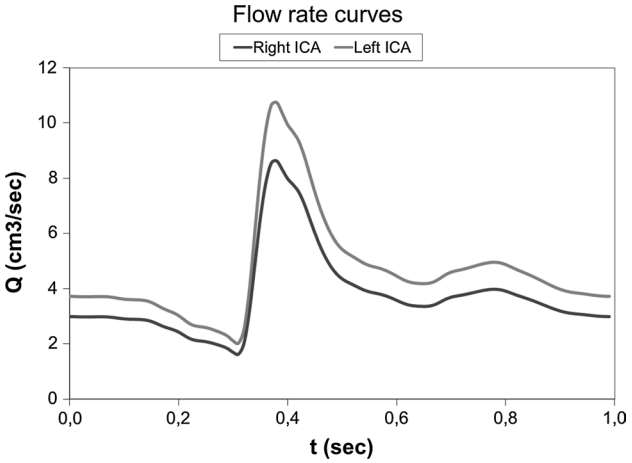

Fig. 1 Flow rate waveform imposed at the inlet of the computational fluid dynamic model of case #5, for both *right* and *left* ICAs having a cross-sectional area of 0.170 and 0.198 cm^2, respectively

were applied at inferior regions to differentiate ICAs from extravascular structures and properly reconstruct parent arteries. The study of these patients was approved by the local institutional review board. However, no patient information was considered in this study. The images were used with the only purpose of reconstructing the vascular models needed to perform the blood flow simulations.

All vascular models were reconstructed using a region-growing segmentation algorithm and isosurface deformable models [9, 31, 42]. An isosurface of triangles is generated by marching cubes algorithm, and serves as a deformable model of the vasculature. The model is deformed by energy minimization, where the energy function is composed of a term derived from the image, and smoothing terms [43]. High-quality unstructured finite element grids of tetrahedra were generated using an advancing front technique [26–28]. Element size was adjusted to roughly maintain the same number of elements in all cross sections, resulting in grids containing up to 2.43 million elements.

2.2 Blood flow numerical simulations

Finite element blood flow simulations were performed using both Newtonian and non-Newtonian Casson rheological models. For the Newtonian runs, blood was modeled as an incompressible fluid with density 1.0 g/cm^3 and viscosity 0.04 Poise. For the Casson model a velocity dependent apparent viscosity was computed from the constitutive equation at every mesh node (1)

$$\mu_{\text{app}} = \left(\sqrt{\tau_0 \frac{1 - e^{-m\dot{\gamma}}}{\dot{\gamma}}} + \sqrt{\mu} \right)^2, \quad (1)$$

where τ_0 is the yield stress, which was assumed as 0.09 g $(\text{cm s})^{-1}$, μ is the Newtonian viscosity and $\dot{\gamma}$ is the shear strain rate. The apparent viscosity to be bonded for any range of shear strain rates when $m > 10$ [5].

The flow dynamics was governed by the 3D unsteady Navier–Stokes equations [30]. Vessel walls were assumed rigid, and non-slip boundary condition was applied at the vascular walls. Pulsatile flow conditions imposed at the inlet of the models were derived from phase-contrast magnetic resonance measurement in a healthy subject. Flow waveforms were scaled according to the ICA cross-sectional area and the principle of minimal work expressed by Murray's law to achieve a mean WSS of 15 $dyne/cm^2$, and imposed at the inflow boundary of each model [33]. Figure 1 shows the normalized flow rate waveform for both ICAs of case #5. The flow rate had been previously acquired using phase-contrast magnetic resonance in a normal volunteer [8]. Fully developed pulsatile velocity profiles were prescribed with use of the Womersley solution [38, 40]. Assuming that all distal vascular beds have similar total resistance to flow, traction-free boundary conditions were applied at the outlets. The Navier–Stokes equations were numerically integrated using a fully implicit finite element formulation [9]. Two cardiac cycles with 100 time-steps per cycle were computed, and all reported results correspond to the second cycle.

2.3 Data reduction and analysis

In order to investigate whether or not Newtonian WSS (WSS_N) is systematically higher than non-Newtonian Casson WSS (WSS_C) in regions of low WSS, maps of WSS magnitude at the end diastole were created for each case. The percent relative difference between both distributions was computed at every grid point, and utilized to

investigate possible correlations between low WSS regions and regions where any of the models predicts lower or higher WSS than the other.

For each case, WSS was also spatially averaged at every time at a region over a selected bleb (lowest WSS), and over the parent artery close to the neck (highest WSS). The location of those regions was derived from the WSS distribution at the systolic peak. At those regions, the dependence of both Casson and Newtonian WSS on time, $\mathrm{WSS_C}(t)$ and $\mathrm{WSS_N}(t)$, was computed and compared. The time-averaged values at those regions for every case and for each rheology, $\langle \mathrm{WSS_C} \rangle$ (2) and $\langle \mathrm{WSS_N} \rangle$ (3), were computed over the cardiac cycle ($T = 1$ s). The relative percent differences $\varepsilon_{\langle \mathrm{WSS} \rangle}$ between $\langle \mathrm{WSS_C} \rangle$ (2) and $\langle \mathrm{WSS_N} \rangle$ were computed for each case at every location (4).

$$\langle \mathrm{WSS_C} \rangle = \frac{1}{T} \int_0^T \mathrm{WSS_C}(t) \mathrm{d}t \tag{2}$$

$$\langle \mathrm{WSS_N} \rangle = \frac{1}{T} \int_0^T \mathrm{WSS_N}(t) \mathrm{d}t \tag{3}$$

$$\epsilon_{\langle \mathrm{WSS} \rangle} = \frac{\langle \mathrm{WSS_C} \rangle - \langle \mathrm{WSS_N} \rangle}{\langle \mathrm{WSS_C} \rangle} \tag{4}$$

For each case, the peak of WSS and the minimum WSS before the systolic peak at selected blebs and the afferent arteries were computed for both viscosity models. The relative percent differences $\varepsilon_{\mathrm{PEAK\ WSS}}$ and $\varepsilon_{\mathrm{MIN\ WSS}}$ were calculated.

In order to determine whether or not the Casson model produce a $\langle \mathrm{WSS} \rangle$, a peak of WSS and a minimum WSS significantly different from those computed using a Newtonian rheology at both the selected blebs and the afferent arteries, two-sample Welche's t tests for independent samples with unknown variances were performed. The approximate degrees of freedom were computed from the standard deviations and the size of the sample using the Satterthwaite's approximation.

The relative differences $D_{\mathrm{WSS}}(t)$ between Casson and Newtonian WSS were also computed for each case at the afferent arteries and the selected blebs (5), and the minimum ($D_{\mathrm{WSS\ min}}$), average ($D_{\mathrm{WSS\ ave}}$) and maximum ($D_{\mathrm{WSS\ max}}$) values were recorded.

$$D_{\mathrm{WSS}}(t) = \frac{\mathrm{WSS_C}(t) - \mathrm{WSS_N}(t)}{\mathrm{WSS_C}(t)} \tag{5}$$

3 Results

Ten cerebrovascular images exhibiting aneurysms containing blebs were considered for this study. The number of

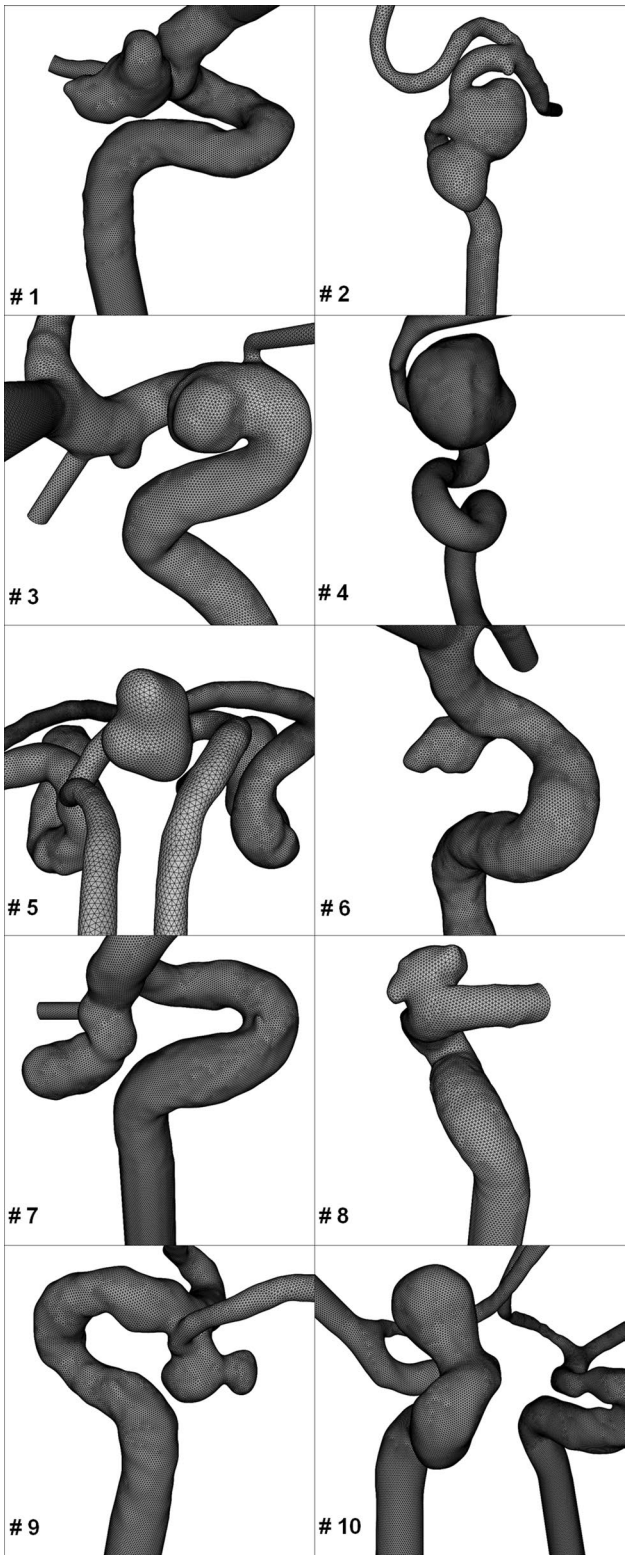

Fig. 2 Computational fluid dynamic grids for cases #1 to #10 reconstructed from angiography images acquired in patients having cerebral aneurysms with blebs

elements in the unstructured tetrahedral grids reconstructed from those images depends on the model size (see Fig. 2). The maximum number of elements was as high as 2.43 million elements for case #5, which contains both left and right vasculatures.

The ⟨WSS⟩ at the afferent artery (Fig. 3) and at the selected bleb (Fig. 4) for both viscosity models and each case is presented. It was observed that $\langle WSS_C \rangle$ at the afferent artery was systematically higher than $\langle WSS_N \rangle$. That difference ranged between 3.7 and 12.3 % (average 7.4 %). At the selected blebs, 4 out of 10 cases showed that $\langle WSS_C \rangle$ was higher than $\langle WSS_N \rangle$. That difference ranged between −23.8 and 70.6 % (average 1.2 %) where positive differences indicate that $\langle WSS_C \rangle$ was higher. It is worth mentioning that for case #9, both $\langle WSS_C \rangle$ and $\langle WSS_N \rangle$ were less than 1 dyne/cm^2, and Casson model predicted a ⟨WSS⟩ value at the bleb 70.6 % higher. On the other hand, in cases #8 and #10, where both $\langle WSS_C \rangle$ and $\langle WSS_N \rangle$ were less than 3 dyne/cm^2, Casson model predicted ⟨WSS⟩ values at the bleb 2.2 and 9.2 % lower, respectively. It was also observed that peak WSS was systematically higher for the Casson rheology at the afferent artery with a mean relative difference of 5.26 %. For the selected bleb, peak WSS was higher for the Casson rheology in 6 out of 10 cases with a mean relative difference of 0.85 %. Regarding the minimum WSS, it was observed that WSS_N was higher in 1 out of 10 cases at the afferent artery, with a mean difference of 6.79 %, and in 3 out of 10 cases at the selected bleb, with a mean difference of 3.20 %. The relative differences $\varepsilon_{\langle WSS \rangle}$, $\varepsilon_{PEAK\ WSS}$, and $\varepsilon_{MIN\ WSS}$ are shown in Table 2. For case #1, the WSS at the bleb was much higher than in the other cases. That is due to the fact that this case corresponds to the smallest aneurysm (0.50 cm) with a small bleb, which is under a higher WSS with respect to the other cases.

When averaging all cases at both the afferent artery and the selected blebs, estimations of ⟨WSS⟩, peak WSS, and the minimum WSS before the systolic peak were higher when the Casson model was considered. In order to determine whether or not $\langle WSS_C \rangle$, peak WSS_C, and the minimum WSS_C are statistically different from $\langle WSS_N \rangle$, peak WSS_N, and the minimum WSS_N, at both the afferent artery and the selected blebs, a total of six two-sample Welche's *t* tests were performed. For all tests, the computed degrees of freedom using the Satterthwaite's approximation was 17, therefore the hypothesis that Casson and Newtonian estimations are equal must be rejected at CI 95 % for test statistics greater than 1.740 or lower than −1.740. Computed test statistics for ⟨WSS⟩ were 0.897 at the afferent artery and 0.023 at the bleb. For the peak WSS those statistics were 1.012 at the artery and 0.037 at the bleb, while for the minimum WSS, were 0.454 at the artery and 0.032 at the bleb. Therefore, none of those quantities reached statistical significance to reject the equal means hypothesis. Test

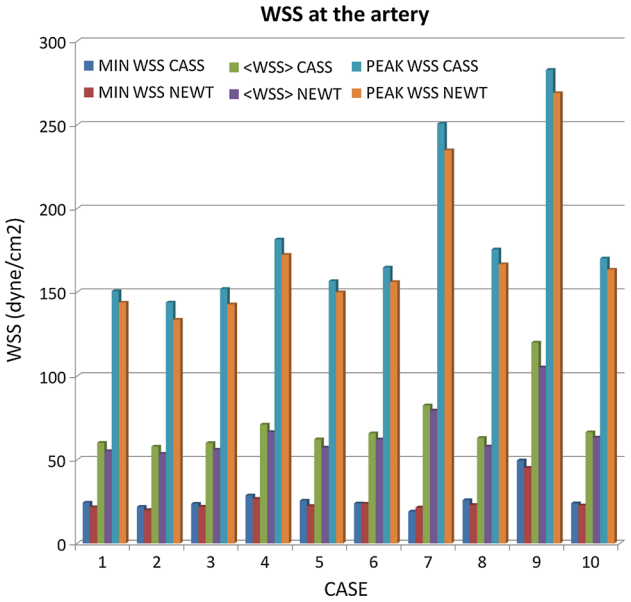

Fig. 3 Minimum, time-average and peak WSS computed using the Casson and the Newtonian rheological models at the artery

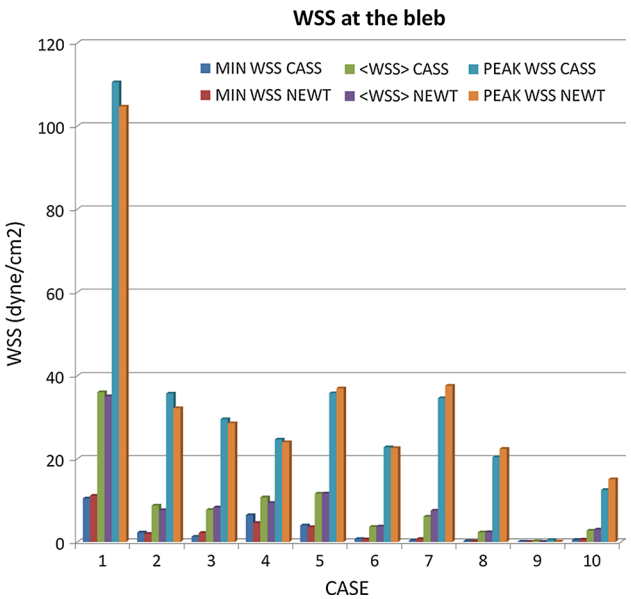

Fig. 4 Minimum, time-averaged and peak WSS computed using the Casson and the Newtonian rheological models at the selected bleb

statistics were higher for the afferent artery because WSS_C was systematically higher than WSS_N.

The WSS distributions at the end diastole were investigated considering both rheological models for cases #1–5 (Fig. 5) and cases #6–10 (Fig. 6). The regions of high and low WSS remain unchanged when comparing in those two figures the Casson (first column) and Newtonian (second column) wall shear stress estimation. In order to

Table 2 Percent differences between the Casson and Newtonian estimation of the time-averaged WSS, the minimum WSS and the peak WSS

Case #	Afferent artery			Bleb		
	$\varepsilon_{\text{MIN WSS}}$	ε_{WSS}	$\varepsilon_{\text{PEAK WSS}}$	$\varepsilon_{\text{MIN WSS}}$	ε_{WSS}	$\varepsilon_{\text{PEAK WSS}}$
1	11.2	8.3	4.5	−6.2	2.7	5.3
2	8.9	7.5	7.0	13.8	12.4	9.9
3	7.5	6.7	6.0	−74.2	−7.9	3.3
4	7.2	6.4	5.1	29.2	12.5	2.7
5	12.6	8	4.3	10.1	−0.3	−3.3
6	0.8	5.5	5.3	11.4	−2.8	0.8
7	−12.8	3.7	6.4	−108.2	−23.8	−8.7
8	11.1	8.2	5.1	5.0	−2.2	−10
9	9.0	12.3	4.9	75.0	70.6	77.1
10	5.4	4.8	4.0	−14.3	−9.2	−20.6

Positive differences indicate that Casson estimation was higher

better visualize the intra-aneurysmal WSS distribution, color map ranges between blue (0.0 dun/cm^2) and magenta (>20.0 dyne/cm^2). The relative difference between absolute values of WSS for the Newtonian and Casson flows is shown in the third column. Color map ranges between blue (where WSS_N doubles WSS_C) to magenta (where WSS_C doubles WSS_N). In darker regions, differences between WSS estimations tend to vanish. For all cases, it is observed that in the arteries, where the flow is higher, WSS_C systematically exceeds WSS_N (dark red). However, those differences are typically less than 50 %, even in regions where the WSS is below 10 dyne/cm^2. In low WSS regions (<10 dyne/cm^2) within the aneurysm sacs, either WSS_C or WSS_N is higher. No systematic pattern was found. While cases #2, #5 and #7 show that WSS_N is higher in most low WSS regions within the aneurysm sac, cases #4, #6, #8 and #9 show that WSS_C does. In the other cases no trend can be derived from the observation of the stress distribution at the end diastole where the lowest WSS values are expected (see Figs. 5, 6).

The variations of ⟨WSS⟩ in time over the selected locations were investigated (Fig. 7 for cases #1–5, Fig. 8 for cases #6–10). For all cases, WSS_C at the afferent artery is higher at every time. At the selected blebs, different results were found. In cases #1, #2 and #9, WSS_C was higher at every time. In cases #3, #7, #8 and #10, WSS_N was higher in the entire cardiac cycle, but either the acceleration or deceleration phase. In the diastolic phase, where lower WSS values are expected, WSS_C was higher in six out of ten cases: cases #1, #5 and #6 (<2 %), case #2 and #4 (<20 %), and case #9 (>300 %). On the other hand, WSS_N was higher in cases #3, #8 and #10 (<20 %) and case #7 (35 %). Table 3 shows the minimum ($D_{\text{WSS min}}$), average ($D_{\text{WSS ave}}$), and maximum ($D_{\text{WSS max}}$) of all $D_{\text{WSS}}(t)$ curves for each case at all locations.

Finally, the time to WSS peak at the blebs and at the afferent artery was computed and compared to that of the flow rate waveform. The WSS at the afferent artery did not exhibit any time shift in any case for any viscosity model. However, at the blebs most cases exhibit a shift 2–10 % of the cardiac cycle. In all cases but case #3, where that shift was 8 % for the Casson model and 10 % for the Newtonian model, no differences were observed when using different rheological models (see Table 3).

4 Discussion

The aim of this work is to investigate WSS spatial and temporal differences when Newtonian and Casson viscosity models are considered, by means of unsteady finite element blood flow simulations in computational domains harboring aneurysms with blebs, under personalized flow conditions based on flow rate normalization according to the principle of minimum biological work, in regions of low and high WSS. When a stationary flow in a rigid and straight pipe is considered, WSS values are larger for a Casson flow. This difference is more significant at lower Reynolds numbers [5, 30]. However, when realistic geometries are considered under pulsatile regimes the differences must be investigated in a patient-specific basis. Rayz et al. [32] found no significant differences between low WSS regions that may be associated with risk of thrombus formation using Newtonian and non-Newtonian computational fluid dynamic simulations in three patients. However, accounting for non-Newtonian behavior improved the agreement with observations using longitudinal MRI studies. Jou et al. [22] found that Newtonian flow overestimate the impingement size in a giant internal carotid artery aneurysm, which may affect predictions based on that parameter. Khanafer et al. [24] showed that non-Newtonian WSS is greater during the peak systole in a limited number of aortic aneurysm models. Valencia et al. [39] investigated the effect of non-Newtonian rheology on the flow pattern of typical aneurysms at the basilar artery and found that the non-Newtonian fluid assumption yields more stable flows than a Newtonian

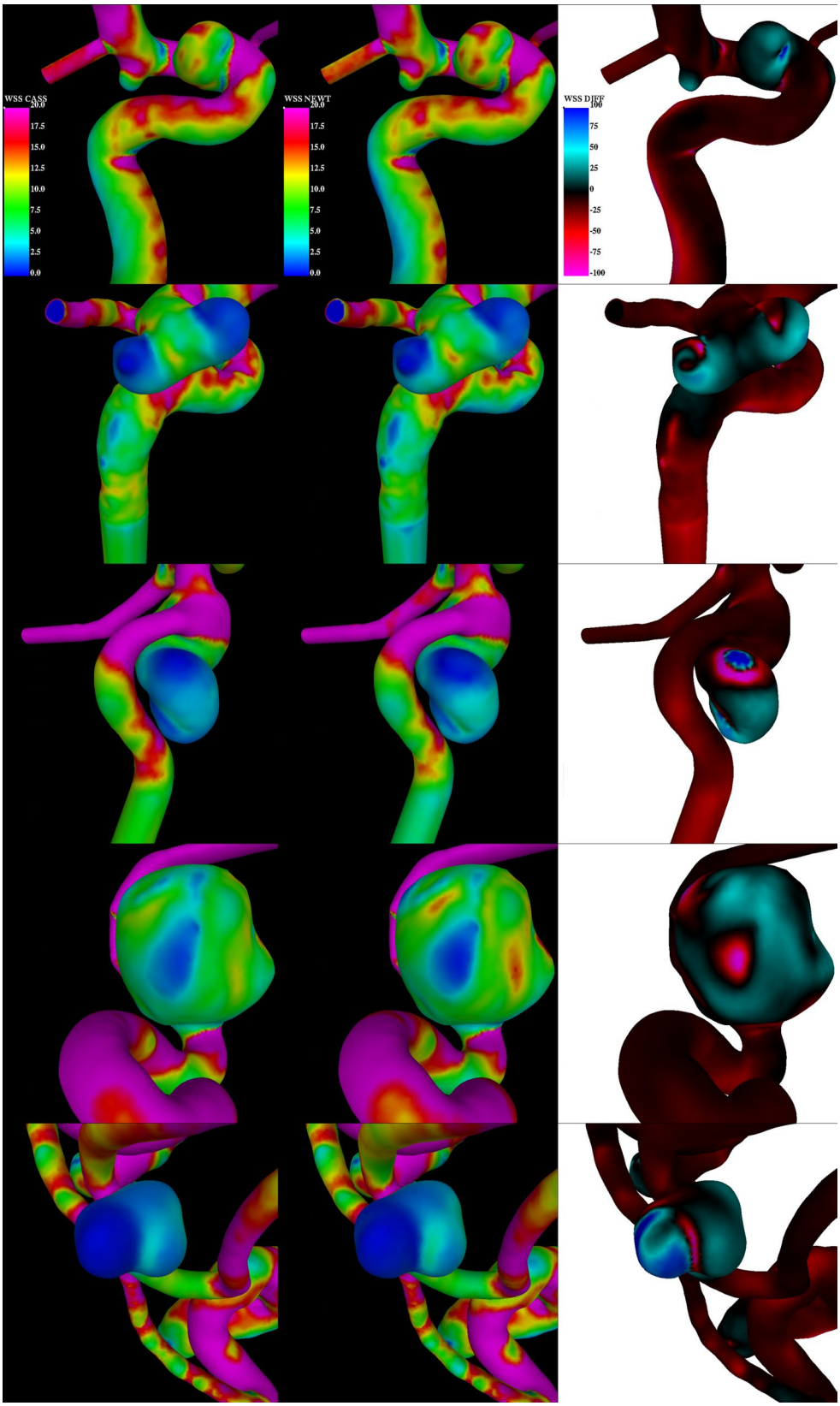

Fig. 5 Wall shear stress analysis at the end diastole for cases #1 to #5. *First column* WSS maps for Casson rheology. WSS range between 0 dyne/cm^2 (*blue*) and 20 dyne/cm^2 (*magenta*); *second column WSS* maps for Newtonian rheology. WSS range between 0 dyne/cm^2 (*blue*) and 20 dyne/cm^2 (*magenta*); *third column* relative difference between the Newtonian and Casson WSS, where *magenta* indicates that WSS_C is as much as twice the WSS_N, *blue* indicates that WSS_N is as much as twice the WSS_C, and *dark regions* correspond to similar WSS values

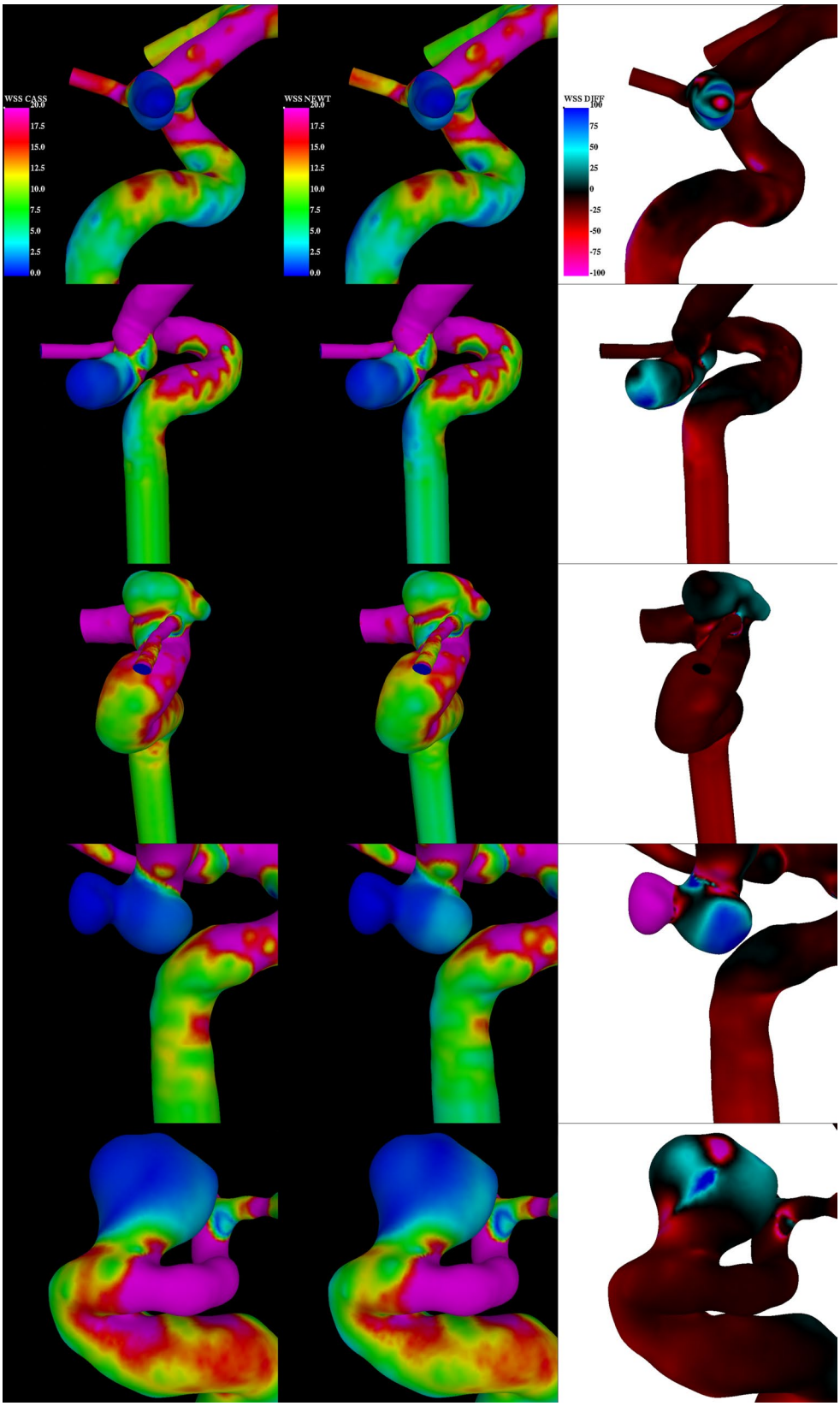

Fig. 6 Wall shear stress analysis at the end diastole for cases #6 to #10. *First column* WSS maps for Casson rheology. WSS range between 0 dyne/cm^2 (*blue*) and 20 dyne/cm^2 (*magenta*); *second column WSS* maps for Newtonian rheology. WSS range between 0 dyne/cm^2 (*blue*) and 20 dyne/cm^2 (*magenta*); *third column* relative difference between the Newtonian and Casson WSS, where *magenta* indicates that WSS_C is as much as twice the WSS_N, *blue* indicates that WSS_N is as much as twice the WSS_C, and *dark regions* correspond to similar WSS values

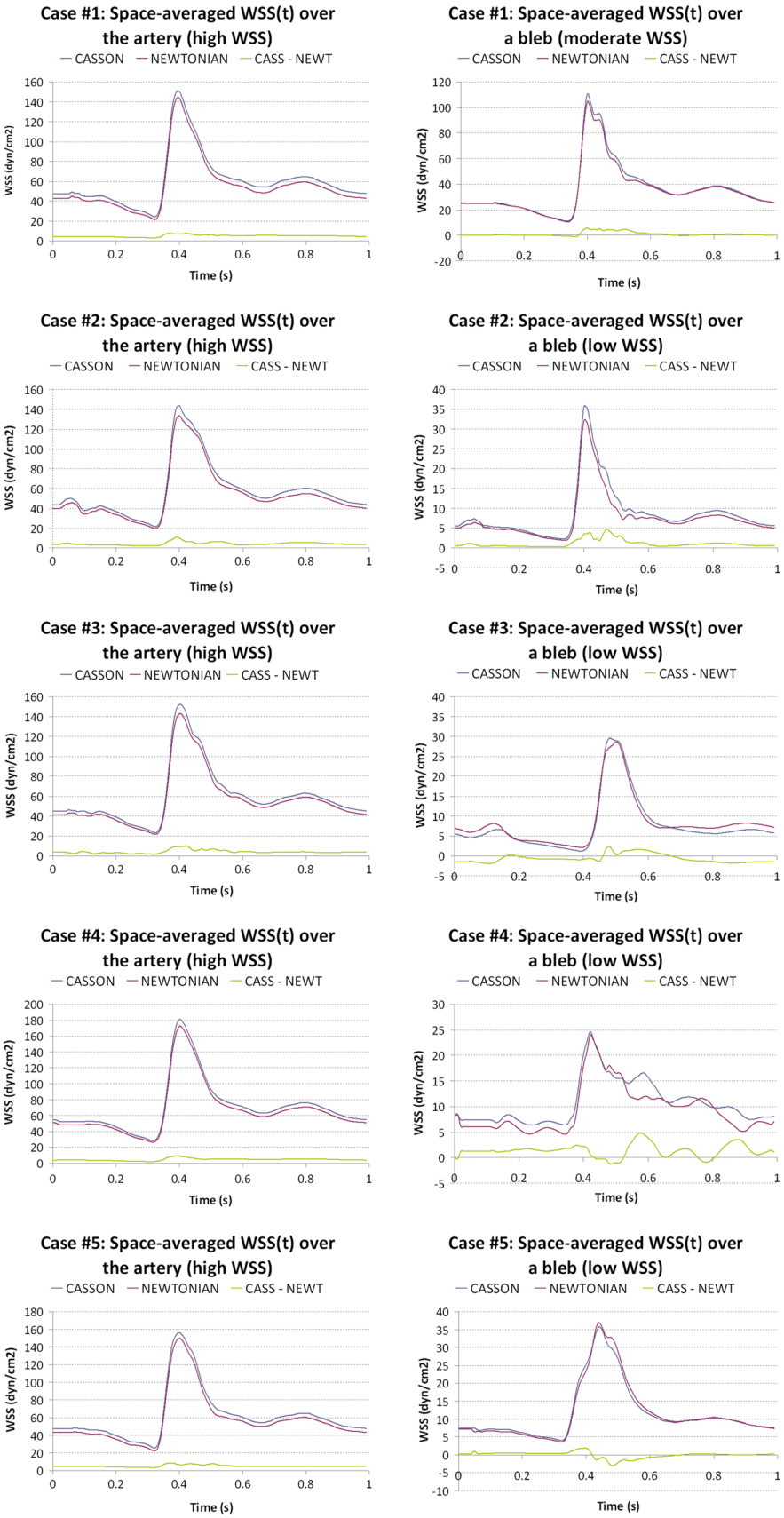

Fig. 7 Time evolution of the WSS averaged at the afferent artery (*left column*) and a selected bleb under low WSS (*right*) along the cardiac cycle computed using Casson (*blue*) and Newtonian (*red*) rheological model, along with the difference $WSS_C - WSS_N$ (*green*), for cases #1 to #5

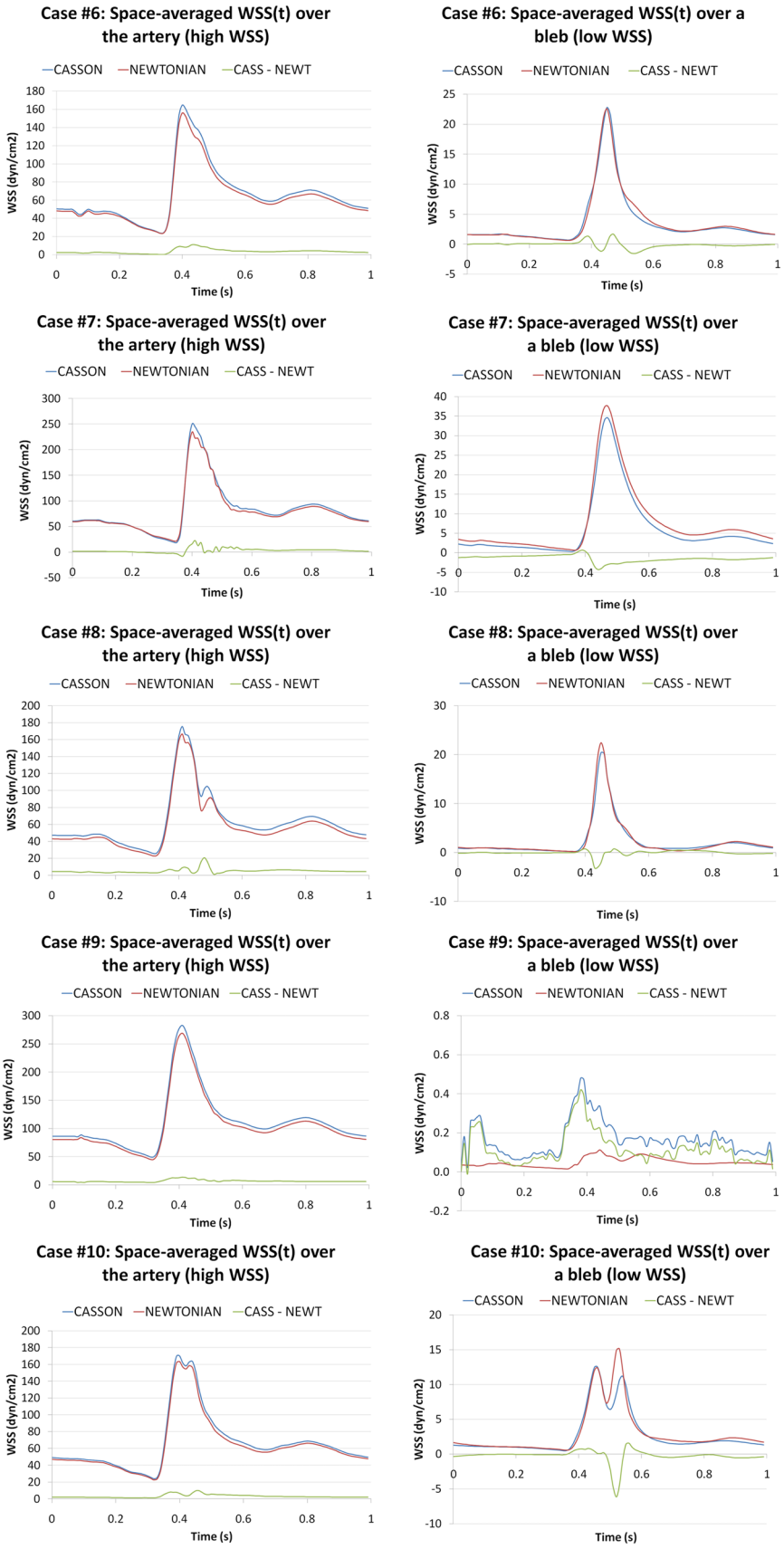

Fig. 8 Time evolution of the WSS averaged at the afferent artery (*left column*) and a selected bleb under low WSS (*right*) along the cardiac cycle computed using Casson (*blue*) and Newtonian (*red*) rheological model, along with the difference $WSS_C - WSS_N$ (*green*), for cases #6 to #10

Table 3 Percent differences between Newtonian and Casson WSS

Case #	Afferent artery				Bleb				Phase shift in WSS peaks (s)	
	Peak WSS location (s)	$D_{WSS}(t)$			Peak WSS location (s)	$D_{WSS}(t)$				
		$D_{WSS\ min}$ (%)	$D_{WSS\ ave}$ (%)	$D_{WSS\ max}$ (%)		$D_{WSS\ min}$ (%)	$D_{WSS\ ave}$ (%)	$D_{WSS\ max}$ (%)	Casson (%)	Newt. (%)
1	C: 0.40 N: 0.40	4.7	9.8	13.2	C: 0.40 N: 0.40	−7.1	1.7	11.1	0	0
2	C: 0.40 N: 0.40	3.8	8.5	11.3	C: 0.40 N: 0.40	6.6	13.7	36.2	0	0
3	C: 0.40 N: 0.40	4.3	7.4	10.5	C: 0.48 N: 0.50	−42.6	−13.0	16.1	8	10
4	C: 0.40 N: 0.40	4.0	7.2	9.4	C: 0.42 N: 0.42	−8.3	19.0	65.3	2	2
5	C: 0.40 N: 0.40	4.7	9.6	14.7	C: 0.44 N: 0.44	−9.5	2.1	16.0	4	4
6	C: 0.40 N: 0.40	0.8	3.6	8.5	C: 0.45 N: 0.45	−24.0	−1.2	34.2	5	5
7	C: 0.40 N: 0.40	−16.3	2.5	12.7	C: 0.47 N: 0.47	−53.5	−28.4	33.4	7	7
8	C: 0.40 N: 0.40	1.5	9.7	25.9	C: 0.44 N: 0.44	−23.2	9.5	129.9	4	4
9	C: 0.40 N: 0.40	4.7	6.9	10.0	C: 0.43 N: 0.43	−32.6	281.4	1,463.0	3	3
10	C: 0.40 N: 0.40	2.3	5.0	9.4	C: 0.46 N: 0.46	−41.3	−8.3	39.7	6	6

Column 1 indicates the case number. Columns 2 and 6 show the location of the WSS peaks (in seconds) where $t = 0$ is the same as in the flow rate curve (Fig. 1), for the afferent artery and the selected bleb, respectively, and for both the Casson (C) and Newtonian (N) rheological models. Columns 10 and 11 show the time shift between those peaks at both the afferent artery and that in the selected bleb for both rheologies. Columns 3–5 and 7–9 show the minimum ($D_{WSS\ min}$), the average ($D_{WSS\ ave}$) and the maximum ($D_{WSS\ max}$) difference $D_{WSS}(t)$ along the cardiac cycle between the Casson and Newtonian WSS at both the afferent artery and the selected blebs. Positive differences indicate that WSS_C was higher

fluid, for the same inlet flow rate. Xiang et al. [41] showed that Newtonian viscosity model could overestimate normalized WSS and consequently underestimate the risk of rupture of intracranial aneurysm in three ICA aneurysms. Fisher et al. studied a given number of rheological models in different idealized aneurysm models. It was found that spatially averaged Newtonian WSS was higher than the corresponding Casson WSS at the aneurysm dome during the whole cardiac cycle. The relative difference was higher during the diastole rather than the systole [20].

In this work, we investigated the WSS in aneurysm blebs (lowest WSS), and at the afferent artery close to the aneurysm neck (highest WSS), using both the Casson and Newtonian rheological models. The first observation is that WSS_C is systematically larger than WSS_N at the afferent arteries, which is compatible with the high flow rates at large arteries. Secondly, the hemodynamic characterization at the end diastole (e.g., high and low WSS zones, WSS distribution, etc.) remain unchanged, which is in agreement with a previous sensitivity study where no difference in the hemodynamic characterization was found at the peak systole [9]. In some cases, limited regions where WSS_N is higher at the end diastole were found. However, that was not the rule. Third, regions under low WSS at the whole or part of the cardiac cycle do not correlate with regions where either WSS_N or WSS_C is higher. When averaging all cases, estimations of $\langle WSS \rangle$, peak WSS and the minimum WSS value before the systolic peak were higher when the Casson model was considered, regardless location. However, Casson estimations were not significantly different from Newtonian ones. Significance is even lower at blebs under lower WSS. Finally, it was found a shift in time of the WSS peaks at the afferent artery and the bleb, which may be associated to the complex intra-aneurysmal flows. The same shift remained the same regardless the viscosity models used. Similar result was previously presented by Jou et al. [22], who found that impingement at the dome occurs approximately 0.11 s after the peak of waveform. They also showed that the time delay increases with the aneurysm size, and varies with the flow waveform and the heart rate.

Based on our results, it cannot be concluded that Newtonian viscosity could overestimate WSS when WSS is low, as suggested by Xiang et al. [41]. Although we observed

that WSS_C is higher in most regions and time intervals, differences are not statistically significant. In our CFD models the flow rate waveform imposed at the inlet of the cerebrovascular models had been acquired in a normal volunteer and were scaled according the ICA cross-sectional area and the principle of minimum biological work. Therefore, no further WSS normalization was required for inter-patient comparability. Additionally, we studied the WSS along the entire cardiac cycle at low and high WSS regions. Instead, Xiang et al. [41] based their analysis on the normalized WSS with respect to the WSS at the afferent artery, and WSS was computed from a time-averaged velocity field.

A previous study showed a possible association between high maximum WSS at the systolic peak and rupture in a cohort of 26 AComA aneurysms [31]. A larger CFD study that considered 210 cerebral aneurysms at different locations including 1,050 CFD simulations reported statistically significant associations within the 95 % CI between aneurysm rupture and larger WSS, smaller impingement regions, larger WSS concentrations, more complex flow patterns, and larger inflow concentrations [13, 15, 18]. Bleb formation also correlated with regions of high WSS [6] or high WSS spatial gradient [14] before aneurysm formation was also reported. In all those and many other similar studies, Newtonian rheology was assumed. Although a larger number of cases should be considered in order to derive a statistical correlation, based on our findings, Casson rheology does not significantly affect the WSS characterization from which conclusions reported in previous works were derived.

5 Conclusion

In this work, personalized computational fluid dynamics modeling was utilized to investigate differences in wall shear stress estimation in vascular domains containing cerebral aneurysms, when different rheological models were considered. In order to characterize those differences, time dependence of wall shear stress was investigated in regions of high and low stresses. Only aneurysms with blebs were considered in order to analyze regions of extremely low wall shear stress. Distributions were also spatially compared at the end systole, where the lowest stresses are expected. Regions where Newtonian estimation of WSS was higher, when present, occurred within the aneurysm sacs. However, their location did not correlate with regions of extremely low WSS. Based on our findings, Newtonian rheology does not systematically overestimate wall shear stress. Furthermore, based on a number of WSS metrics, and a limited number of ten cases, both approximations are not significantly different. Therefore, these results suggest that previously reported results based on a Newtonian viscosity are not expected to change if a Casson model had been considered.

Acknowledgments Marcelo Castro wants to acknowledge CONICET (Consejo Nacional de Investigaciones Científicas y Técnicas, Argentina) for financial support. This work was partially supported by research Grant PICT #2012-279 ANPCyT (Agencia Nacional de Promoción Científica y Tecnológica, Argentina).

References

1. Antiga L, Piccinelli M, Botti L, Ene-Iordache B, Remuzzi A, Steinman DA (2008) An image-based modeling framework for patient-specific computational hemodynamics. Med Biol Eng Comput 46(11):1097–1112
2. Cárdenes R, Larrabide I, Frangi AF, Román LS (2013) Performance assessment of isolation methods for geometrical cerebral aneurysm analysis. Med Biol Eng Comput 51(3):343–352
3. Castro MA (2013) Understanding the role of hemodynamics on the initiation, progression, rupture, and treatment outcome of cerebral aneurysm from medical image-based computational studies. ISRN Radiol 2013:1–17
4. Castro MA, Putman CM, Cebral JR (2006) Computational fluid dynamics modeling of intracranial aneurysms: effects of parent artery segmentation on intraaneurysmal hemodynamics, Am J Neuroradiol 27:1703–1709. doi:10.5402/2013/602707
5. Castro MA, Putman CM, Cebral JR (2008) Computational hemodynamics of cerebral aneurysms: assessing the risk of rupture from hemodynamic patterns. VDM Verlag, Germany
6. Castro MA, Putman CM, Cebral JR (2009) Hemodynamic patterns of anterior communicating artery Aneurysms: a possible association with rupture. Am J Neuroradiol 30(2):297–302
7. Castro MA, Ahumada Olivares MC, Putman C, Cebral JR (2013) Hemodynamic differences in intracranial aneurysm blebs due to blood rheology. J Phys Conf Ser 477(012001):1–10. doi:10.1088/1742-6596/477/1/012001
8. Cebral JR, Castro MA, Soto O et al (2003) Blood flow models of the circle of Willis from magnetic resonance data. J Eng Math 47(3–4):369–386
9. Cebral JR, Castro MA, Appanaboyina S et al (2005) Efficient pipeline for image-based patient-specific analysis of cerebral aneurysms hemodynamics: technique and sensitivity. IEEE Trans Med Imaging 24(4):457–467
10. Cebral JR, Pergolizzi RS, Putman CM (2007) Computational fluid dynamics modeling of intracranial aneurysms: qualitative comparison with cerebral angiography. Acad Radiol 14:804–813
11. Cebral JR, Castro MA, Putman CM et al (2008) Flow–area relationship in internal carotid and vertebral arteries. Phys Meas 29(10):585–594
12. Cebral JR, Putman CM, Alley MT, Hope T, Bammer R, Calamante F (2009) Hemodynamics in normal cerebral arteries: qualitative comparison of 4D phase-contrast magnetic resonance and image-based computational fluid dynamics. J Eng Math 64(4):367–378
13. Cebral JR, Sheridan M, Putman CM (2010) Hemodynamics and bleb formation in intracranial aneurysms. Am J Neuroradiol 31:304–310
14. Cebral JR, Mut F, Weir J, Putman CM (2011) Quantitative characterization of the hemodynamic environment in ruptured and unruptured brain aneurysms. Am J Neuroradiol 32:145–151
15. Cebral JR, Mut F, Weir J et al (2011) Association of hemodynamic characteristics and cerebral aneurysm rupture. Am J Neuroradiol 32:264–270

16. Chang HH, Duckwiler GR, Valentine DJ, Chu WC (2009) Computer-assisted extraction of intracranial aneurysms on 3D rotational angiograms for computational fluid dynamics modeling. Med Phys 36(12):5612–5621
17. Chien A, Tateshima S, Castro MA, Sayre J, Cebral JR, Viñuela F (2008) Patient-specific computational flow analysis of brain aneurysms at a single location: comparison of hemodynamic characteristics in small aneurysms. Med Biol Eng Comput 46:1113–1120
18. Crompton M (1996) Mechanisms of growth and rupture in cerebral berry aneurysms. Br Med J 1:1138–1142
19. Evjua O, Valen-Sendstada K, Mardal K-A (2013) A study of wall shear stress in 12 aneurysms with respect to different viscosity models and flow conditions. J Biomech 46:2802–2808. doi:10.1016/j.jbiomech.2013.09.004 (Epub 2013 Sep 16)
20. Fisher C, Stroud Rossmann J (2009) Effects of non-Newtonian behavior on hemodynamics of cerebral aneurysms. J Biomech Eng 131(9):1–9. doi:10.1115/1.3148470
21. Hernández M, Frangi A (2007) Non-parametric geodesic active regions: method and evaluation for cerebral aneurysms segmentation in 3DRA and CTA. Med Image Anal 11:142–224
22. Jou L-D, Mawad ME (2011) Timing and size of flow impingement in a giant intracranial aneurysm at the internal carotid artery. Med Biol Eng Comput 49(8):891–899
23. Jou LD, Lee DH, Morsi H et al (2008) Wall shear stress on ruptured and unruptured intracranial aneurysms at the internal carotid artery. Am J Neuroradiol 29:1761–1767
24. Khanafer KM, Gadhoke P, Berguer R et al (2006) Modeling pulsatile flow in aortic aneurysms: effect on non-Newtonian properties of blood. Biorheology 43:661–679
25. Kulcsar Z, Ugron A, Marosfo M et al (2008) Hemodynamics of cerebral aneurysm initiation: the role of wall shear stress and spatial wall shear stress gradient. Am J Neuroradiol 32(3):587–594. doi:10.3174/ajnr.A2339
26. Löhner R (1996) Extensions and improvements of the advancing front grid generation technique. Commun Numer Method Eng 12:683–702. doi:10.1002/(SICI)1099-0887(199610)12:10<683:AID-CNM983>3.0.CO;2-1
27. Löhner R (1996) Regridding surface triangulations. J Comput Phys 126:1–10
28. Löhner R (1997) Automatic unstructured grid generators. Finite Elem Anal Des 25:111–134
29. Low M, Perktold K, Raunig R (1993) Hemodynamics in rigid and distensible saccular aneurysms: a numerical study of pulsatile flow characteristics. Biorheology 30:287–298
30. Mazumdar JN (1992) Biofluid mechanics. World Scientific, Singapore
31. Nakatani H, Hashimoto N, Kang H et al (1991) Cerebral blood flow patterns at major vessel bifurcations and aneurysms in rats. J Neurosurg 74:258–262
32. Rayz VL, Boussel L, Lawton MT et al (2011) Numerical modeling of the flow in intracranial aneurysms: prediction of regions prone to thrombus formation. Ann Biomed Eng 36(11):1793–1804
33. Sherman TF (1981) On connecting large vessels to small. The meaning of Murray's law. J Gen Physiol 78:431–453
34. Shojima M, Oshima M, Takaqi K et al (2004) Magnitude and role of wall shear stress on cerebral aneurysm: computational fluid dynamic study of 20 middle cerebral aneurysms. Stroke 35:2500–2505
35. Shojima M, Nemoto S, Morita A et al (2010) Role of shear stress in the blister formation of cerebral aneurysms. Neurosurgery 67(5):1268–1275
36. Steinman DA, Milner JS, Norley CJ et al (2003) Image-based computational simulation of flow dynamics in a giant intracranial aneurysm. Am J Neuroradiol 24(4):559–566
37. Steinman DA, Milner JS, Norley CJ et al (2003) Image-based computational simulation of flow dynamics in a giant intracranial aneurysm. Am J Neuroradiol 24:559–566
38. Taylor CA, Hughes TJR, Zarins CK (1998) Finite element modeling of blood flow in arteries. Comput Meth Appl Mech Eng 158:155–196
39. Valencia AA, Guzmán AM, Finol EA et al (2006) Blood flow dynamics in saccular aneurysm models of the basilar artery. J Biomech Eng 128(4):516–526
40. Womersley JR (1955) Method for the calculation of velocity, rate of flow and viscous drag in arteries when the pressure gradient is known. J Physiol 127:553–563
41. Xiang J, Tremmel M, Kolega J et al (2011) Newtonian viscosity model could overestimate wall shear stress in intracranial aneurysm domes and underestimated rupture risk. J Neurointerv Surg 4(5):351–357
42. Yim P, Vasbinder GB, Ho VB et al (2003) Isosurfaces as deformable models for magnetic resonance angiography. IEEE Trans Med Imaging 22(7):875–881
43. Yim P, Demarco KJ, Castro MA, Cebral JR (2005) Characterization of shear stress on the wall of the carotid artery using magnetic resonance imaging and computational fluid dynamics. Stud Health Technol Inform 113:412–442